Refractive-index sensing based on large negative Goos-Hänchen shifts of a wavy dielectric grating

Ma Luo* and Feng Wu

School of Optoelectronic Engineering, Guangdong Polytechnic Normal University, Guangzhou, 510665, China

(Received 5 January 2024; revised 16 May 2024; accepted 21 June 2024; published 19 July 2024)

A wavy dielectric grating hosts bound states in the continuum (BICs) at nonzero Bloch wave number. For an oblique incident optical field with parameters near to the BICs, the reflectance spectrum exhibits an ultrasharp Fano line shape, and the reflected beam has a large negative Goos-Hänchen shift, due to excitation of the corresponding quasi-BIC with negative group velocity. Under incidence of a Gaussian beam with a sizable beam width, the excited quasi-BIC could travel a long distance along the direction of the Goos-Hänchen shift, designated as L_{GH}, before the energy is completely radiated. If the length between the termination of the wavy shape and the focus of the incident Gaussian beam is smaller than L_{GH}, sizable energy flux can be coupled into the waveguide mode of the flat dielectric slab that is connected to the wavy dielectric grating. Measurement of the energy flux of the waveguide mode can sense the variation of the refractive index of the background medium. The proposed sensing scheme can be integrated with a waveguide in an optical circuit.

DOI: 10.1103/PhysRevApplied.22.014050

I. INTRODUCTION

Refractive index sensing based on optical response is the most-efficient means of detecting environmental changes, such as a change of humidity [1] or gas concentration [2]. The critical factors for an efficient sensor are the sensitivity, the figure of merit (FOM), and the ability to be integrated with a photonic circuit. The sensitivity can be increased by various types of optical resonances, such as surface plasmon polaritons (SPPs) and localized surface plasmon resonances (LSPRs) [3–13]. Although SPPs and LSPRs in metallic nanostructures can highly localize the optical field, and then increase the sensitivity, the absorption losses at visible and near-infrared wavelengths reduce the Q factor of the resonant mode [14]. Thus, the figures of merit of sensors based on SPPs and LSPRs are not very high. Sensors based on fully dielectric structures, such as resonant nanocavities in 2D photonic crystals [2] or dielectric gratings [15], have ultralow absorption losses, so the Q factor can be high, and then the FOM can be increased.

A bound state in the continuum (BIC) is a type of localized eigenmode whose resonant frequency lies in the continuous spectrum of radiative optical modes [16–25]. Because the BIC does not couple with the radiative mode, an incident optical field cannot excite the BIC. By one tuning the structural parameter, the BIC can be transformed into a quasi-BIC with an ultrahigh but finite Q factor, which couples with the radiative mode. Under incidence of a plane wave with fixed wavelength, the angular reflectance spectrum (i.e., reflectance versus incident angle) of the dielectric structure with a quasi-BIC exhibits a ultranarrow Fano line shape, so a refractive index sensor based on a quasi-BIC could have a large FOM [15]. For a realistic sensor, the incident optical field is a Gaussian beam instead of a plane wave, so the measured angular reflectance spectrum is the convolution between the Fano line shape and the angular spectrum of the incident Gaussian beam. If the beam width of the Gaussian beam is small, the width of the incident angular spectrum is larger than the width of the Fano line shape, so the width of the measured angular reflectance spectrum is larger than that of the Fano line shape. Thus, the FOM is decreased. On the other hand, if the beam width of the incident Gaussian beam is very large, the FOM is preserved, but the measurement of the reflected or transmitted power requires a detector with a large cross section, which increases the difficulty of integrating the sensor with a photonic circuit.

Another feature of a quasi-BIC is the enhancement of the Goos-Hänchen shifts [26,27], which are lateral shifts of the reflected and transmitted beams from the incident beam. The Goos-Hänchen shifts can also be enhanced by the presence of other types of resonant microstructure [28], such as surface plasmon resonators [29], metal-cladding waveguides [30], ϵ-near-zero metamaterial slabs [31,32], and photonic crystal surface structures [33–36].

In this paper, we propose a refractive index sensor based on large negative Goos-Hänchen shifts of quasi-bound-states-in-the-continuum (quasi-BICs). The sensing signal

*Contact author: luoma@gpnu.edu.cn

 © 2024 American Physical Society

is the energy flux of the waveguide mode, so the sensor can be integrated with a photonic circuit. The structure consists of a dielectric slab in the x-y plane, as shown in Fig. 1(a). Within a finite region $x \in [-N_t a, N_t a]$, the dielectric slab has a wavy structure along the x direction, with a being the period of the wavy structure and N_t characterizing the size of the grating. In the region with $|x| > N_t a$, the dielectric slab is flat. In the region with $(N_t - 3)a < |x| < N_t a$, the magnitude of the wavy shape smoothly decreases to zero. The wavy dielectric grating within the region with $|x| < (N_t - 3)a$ hosts BICs at nonzero Bloch wave number, so in-plane oblique incidence of an optical field could excite the corresponding quasi-BICs [37]. According to the stationary-phase method [27], the Goos-Hänchen shifts assisted by the quasi-BICs are large [38,39]. The quasi-BICs of a wavy dielectric grating have negative group velocity, so the Goos-Hänchen shifts are negative. Assuming that the focus of the incident Gaussian beam is at $x = 0$, the incident field excites a wave packet consisting of quasi-BICs with energy flux along the $-\hat{x}$ direction. As the excited wave packet travels to the region with $x < 0$, the optical field couples into the radiative modes, which form reflected and transmitted beams with negative Goos-Hänchen shifts, as designated by the red arrow $P_{r,-}$ in Fig. 1(a). If $N_t a$ is smaller than sum of the Goos-Hänchen shift and the reflected beam width, the energy of the wave packet is not completely radiated before it reaches $x = -N_t a$, but is partially coupled into the waveguide mode of the flat dielectric slab in the region with $x < -N_t a$, as designated by the red arrow P_{WG} in Fig. 1(a). In our proposed systems, the magnitude of the negative Goos-Hänchen shift is larger than the beam width of the incident Gaussian beam, so the termination of the wavy shape at $x = -N_t a$ does not influence the interaction between the incident Gaussian beam and the wavy dielectric grating. Thus, the large negative Goos-Hänchen shift is preserved, and then P_{WG} is sizable. Measurement of P_{WG} by an integrated photonic detector can be applied as a sensing signal of the refractive index in the background medium. In contrast to previous work reported in Refs. [38,39], we applied a Gaussian beam in real space to excite the quasi-BIC with a large negative Goos-Hänchen shift, so that the sensing signal is the energy flux in the integrated waveguide, instead of the reflected (transmitted) plane wave or Gaussian beam.

The remainder of this paper is organized as follows. In Sec. II, the reflectance spectrum, sensitivity, and FOM under plane-wave incidence for the structure with $N_t = \infty$ are investigated. In Sec. III, the Goos-Hänchen shifts of two selected quasi-BICs are calculated by the stationary-phase method; the Goos-Hänchen shifts in real space for the structure with finite N_t under incidence of a Gaussian beam with a finite beam width are calculated; the sensing scheme based on measurement of the tunneling energy into the flat waveguide is discussed. In Sec. IV, conclusions are presented.

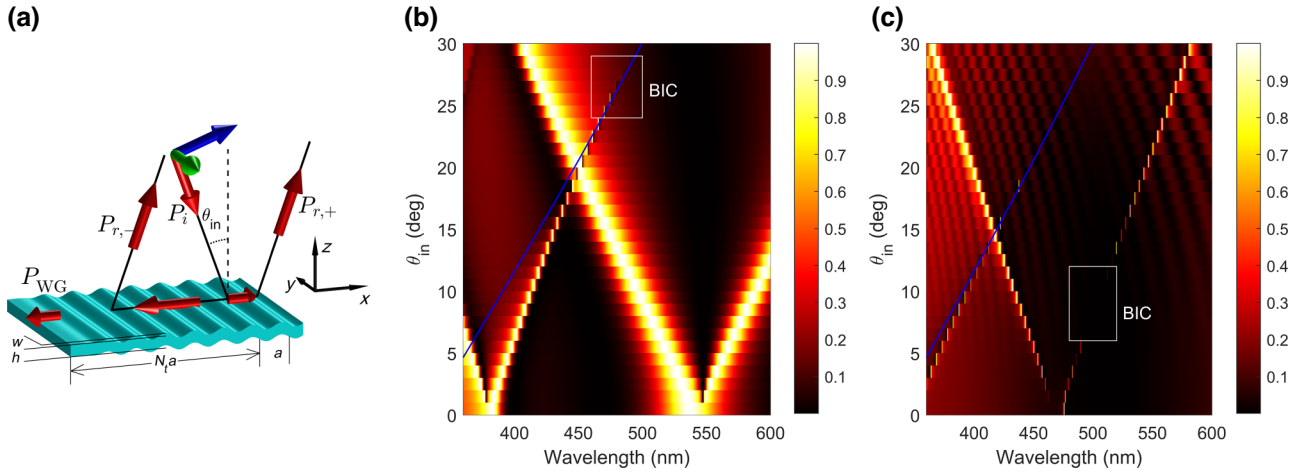

FIG. 1. (a) Structure of the wavy dielectric grating, and scheme of sensing based on an in-plane oblique incident Gaussian beam. The red arrows indicate the main path of the incident optical beam. The power flux of the incident beam is designated as P_i. The power flux of the reflected beams with positive and negative Goos-Hänchen shifts are designated as $P_{r,+}$ and $P_{r,-}$, respectively. The power flux that couples into the flat waveguide adjacent to the left termination of the wavy shape is designated as P_{WG}. The green and blue arrows indicate the linearly polarized directions of the s-polarized and p-polarized incident wave, respectively. (b),(c) Reflectance spectrum of an in-plane oblique incident plane wave with respect to wavelength and incident angle. The blue line marks the relation $(2\pi/a) - k_x = k_0$, which separates the regimes that can and cannot have second-order reflection at angle $-\sin^{-1}(\lambda/a - \sin\theta_{\mathrm{in}})$. The spectra in (b),(c) are for the incidence of an s-polarized and a p-polarized plane wave, respectively. The BICs in (b),(c) are marked by the white rectangles.

II. OPTICAL RESPONSE UNDER PLANE-WAVE INCIDENCE

The structure of the wavy dielectric grating consists of a periodically corrugated dielectric slab with thickness h, as shown in Fig. 1(a). Assuming that the slab lies in the x-y plane, the shapes of the top and bottom surfaces of the dielectric slab within the region $|x| < N_t a$ are given by the function $z = w\sin(2\pi x/a)f(x) \pm h/2$, where w is the magnitude of the corrugation and $f(x) = (1 + \tanh[2(x/a - 1.5 + N_t)])(1 - \tanh[2(x/a + 1.5 - N_t)])/4$ is a smooth ladder function at the two terminations of the wavy shapes. The wavy shapes can be fabricated by application of the femtosecond-laser direct-writing technique [40]. In this section, the scattering of an oblique incident plane wave, whose plane of incidence is the x-z plane, is studied. The wave equations for the electric field (E_y) and the magnetic field (H_y) for the s-polarized and p-polarized incident wave are numerically solved by the spectral-element method [41–46], respectively. In the numerical simulation, the structural parameters are $a = 333$ nm, $h = 134$ nm, and $w = 30$ nm. N_t is infinitely large, so a periodic boundary condition of one period can be applied to simulate the plane-wave scattering. The refractive index n of the dielectric slab is 2. The refractive index of the background medium above the wavy dielectric grating is 1, and that below the wavy dielectric grating denoted n_{sen}. We firstly discuss the case with $n_{\text{sen}} = 1$, and then we study the sensitivity of the optical response to the changing of n_{sen}.

A. Reflectance spectrum

The numerical results for the reflectance spectra for s-polarized and p-polarized incident plane waves in the parameter space of the wavelength (λ) and the incident angle (θ_{in}) are plotted in Figs. 1(b) and 1(c), respectively. Within the white rectangle in Figs. 1(b) and 1(c), the linewidth of the reflectance spectra approaches zero, which implies the existence of a BIC. The thin blue line corresponds to the folded light cone given by $(2\pi/a) - k_x = k_0$, with $k_0 = 2\pi/\lambda$ and $k_x = \sin\theta_{\text{in}} k_0$.

For the s-polarized wave, four bands of leaky resonant modes are identified in Fig. 1(b), which correspond to the band structure above the light cone. In the absence of the wavy shape (i.e., $w = 0$), the flat dielectric slab possesses waveguide modes whose dispersion relations are plotted as dotted lines in Fig. 2(a). The dotted green and black lines are for the first and second waveguide modes, respectively. By our imposing the discrete periodical boundary condition, the dispersion relation of the waveguide modes is folded into the first Brillioun zone, which forms a band structure of the waveguide modes. Specifically, the cutoff mode of the second waveguide band is folded into the first Brillioun zone, so the mode is at the folded light cone given by $(2\pi/a) - k_x = k_0$, as shown by the black circle in Figs. 2(a) and 2(b). As w becomes nonzero, the perturbation modifies the band structure of the waveguide modes, and transfers the modes above the light cone into leaky resonant modes. The band structures of the leaky resonant modes, which are plotted as thick solid lines in Figs. 2(a) and 2(b), can be obtained by one solving the eigenvalue problem of the unit cell with radiative boundary conditions at the top and bottom surfaces. The band crossings of the waveguide modes at $k_x = 0$ are transferred into avoid crossings. In each avoid crossing, one of the two modes is a symmetry-protected BIC with a real eigenvalue. The perturbation induces coupling between the waveguide mode near the cutoff frequency of the second waveguide band and the propagating mode at the light cone, which modifies the band structure near the cutoff frequency of the second waveguide mode. The band structure becomes lower than the dispersion of the waveguide mode,

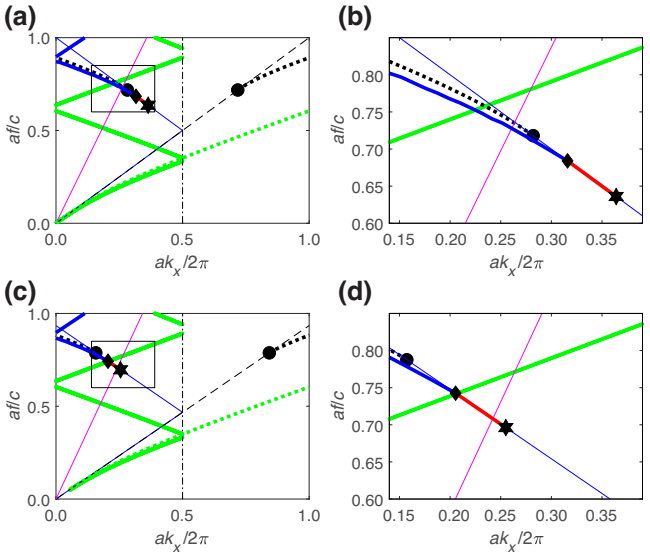

FIG. 2. Band structure of the s-polarized leaky resonant modes with (a),(b) $n_{\text{sen}} = 1$ and (c),(d) $n_{\text{sen}} = 1.07$. (b),(d) Enlargements of (a),(b), respectively, within the rectangular area. The thin dashed black line is the light cone of the lower half space given by $k_x = 2\pi f n_{\text{sen}}/c$. The thin solid blue line is the folded light cone within the first Brillouin zone. The thick dotted green (black) lines below the light cone are the first (second) waveguide dispersion of a flat dielectric slab with $w = 0$ nm. The cutoff mode of the second waveguide mode is marked by the black circle. The second waveguide mode and its cutoff mode are formally folded into the first Brillouin zone. The thick green line and the thick blue-red line are the band structure of the first and second leaky resonant modes of the wavy dielectric grating, which originates from the first and second waveguide dispersion, respectively. The band structure of the second leaky resonant mode crosses the folded light cone at the diamond, and terminates at the hexagram. The thin solid magenta line is the light line given by $k_x = (2\pi f/c)\sin\theta_{\text{in}}$.

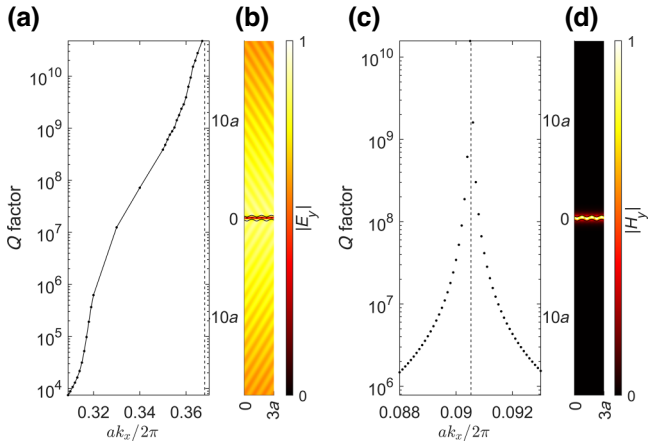

FIG. 3. Q factor versus k_x of the quasi-BIC for (a) s polarization and (c) p polarization. The field patterns of $|E_y|$ and $|H_y|$ of the s-polarized and p-polarized BICs are plotted in (b),(d), respectively.

as shown by the thick blue line in Figs. 2(a) and 2(b). At the diamond with $ak_x/2\pi = 0.316$, the band structure crosses the folded light cone. As k_x further increases, the band structure further extends with frequency slightly above the folded light cone, as shown by the thick red line in Figs. 2(a) and 2(b). The band structure terminates at the hexagram, with the wave number being $ak_{x,c\mathrm{BIC}}/2\pi = 0.3681$, with cBIC standing for the cutoff-BIC to be defined. The Q factors of the leaky resonant modes along the band structure (from the thick blue line to the thick red line) are plotted in Fig. 3(a). As k_x approaches $k_{x,c\mathrm{BIC}}$, the Q factor increases and approaches infinity, which implies that the resonant mode at $k_{x,c\mathrm{BIC}}$ is a BIC. We designated the BIC as the cutoff BIC, because the BIC originates from the cutoff waveguide mode. The field pattern of a quasi-BIC at $ak_x/2\pi = 0.36$ is plotted in Fig. 3(b), and is highly nonlocalized. Because the field pattern of the BIC and the corresponding quasi-BICs is highly nonlocalized, a unit cell with large size along the z direction is required in the numerical calculation to obtain an accurate result. For a quasi-BIC at k_x, the field pattern can be decomposed into the superposition of a series of Fourier modes with Bloch wave number $k_x - N_w 2\pi/a$ (with N_w being an integer). The Fourier mode with $k_x - 2\pi/a$ is near the light cone, whose evanescent field is nearly nonlocalized. Because the quasi-BIC originates from the coupling between the propagating mode at the light cone and the waveguide mode, the superposition coefficient of the Fourier mode with wave number $k_x - 2\pi/a$ is sizable. Thus, the field pattern is highly nonlocalized. As k_x approaches $k_{x,c\mathrm{BIC}}$, the Q factor of the quasi-BIC approaches infinity with a varying rate, i.e., $Q \propto 1/|k_x - k_{x,c\mathrm{BIC}}|^p$ with a varying index p. This phenomenon might be due to the high delocalization of the field pattern.

Under plane-wave incidence, the reflectance spectrum has a resonant peak near the crossing point between the band structure and the light line given by $k_x = k_0 \sin\theta_{\mathrm{in}}$. As $\theta_{\mathrm{in,BIC}} > 28^\circ$, the resonant peak becomes ultrasharp, because the Q factor of the leaky resonant mode at the crossing point is larger than 10^6. The group velocity of the quasi-BICs is negative, because the slope of the corresponding band structure is negative.

For the p-polarized wave, three bands of leaky resonant modes are identified in Fig. 1(c). The band structure near the blue line consists of the quasi-BICs corresponding to the cutoff BIC, which has a feature similar to that of the s-polarized wave. Another BIC is identified with wavelength $\lambda_{\mathrm{BIC}} = 506$ nm and incident angle $\theta_{\mathrm{in,BIC}} = 9^\circ$, which is marked by the white rectangle. The Q factors of the corresponding quasi-BICs are plotted versus the wave number in Fig. 3(c), and satisfy the condition $Q \propto 1/|k_x - k_{x,\mathrm{BIC}}|^2$. Thus, the BIC is a typical accidental BIC. The field pattern of the accidental BIC is plotted in Fig. 3(d), and is highly localized within the wavy dielectric slab. The group velocity of the corresponding quasi-BICs is also negative.

B. Sensitivity and FOM under plane-wave incidence

Changing n_{sen} changes the resonant frequency of the BICs, which in turn changes the reflectance spectra of the corresponding quasi-BICs. In other words, the wavelength of the reflectance peak of the quasi-BIC is sensitive to the change of refractive index. The sensitivity of the reflectance peak to n_{sen} is defined as [47,48]

$$S = \frac{d\lambda_{\mathrm{peak}}}{dn_{\mathrm{sen}}}, \tag{1}$$

and the FOM is defined as

$$F = \frac{S}{\Delta\lambda_{\mathrm{peak}}}, \tag{2}$$

where λ_{peak} is the wavelength at the peak of the reflectance and $\Delta\lambda_{\mathrm{peak}}$ is the full width at half maximum (FWHM) of the peak.

For the s-polarized wave, as n_{sen} increases, the slope of the light cone of the lower half space decreases, and the frequency of the cutoff BIC increases, as shown in Figs. 2(c) and 2(d). The band structure of the quasi-BIC corresponding to the cutoff BIC shifts to the regime with larger frequency and smaller k_x. Consequently, the frequency of the crossing point between the light line with a fixed incident angle θ_{in} and the band structure decreases. When n_{sen} is slightly larger than 1, the crossing point is at the blue section of the band structure, which corresponds to the quasi-BIC with a moderate Q factor. In this case, the resonant peak of the reflectance spectrum has a sizable FWHM, so the FOM is small. When the increase of n_{sen} is large enough, the crossing point is at the red section of

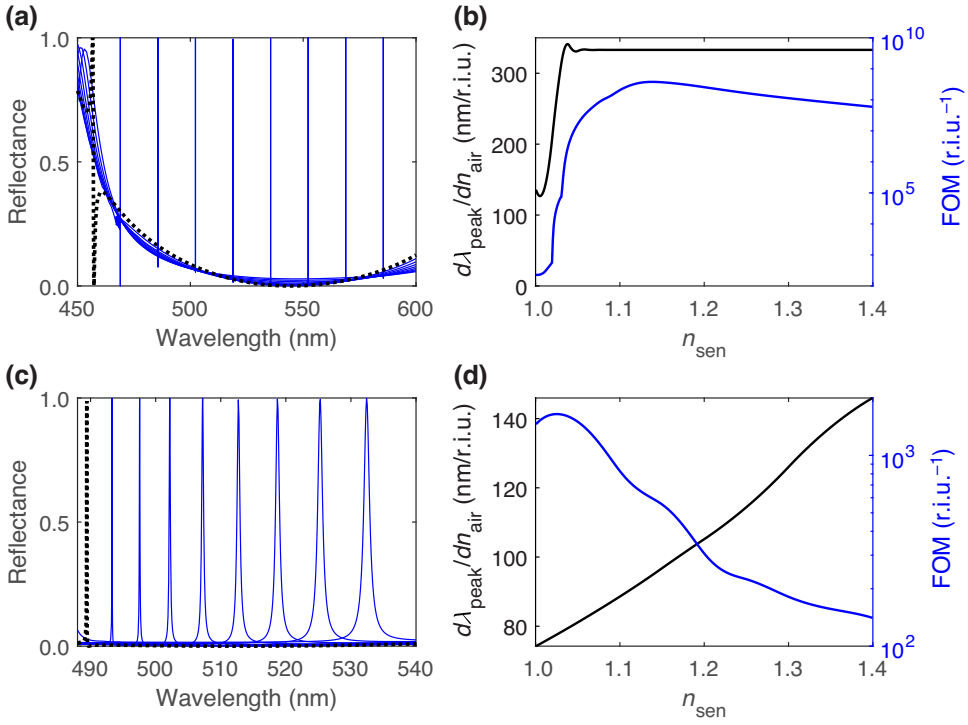

FIG. 4. (a),(c) Numerical results for reflectance spectra of the incident plane wave. In each figure, the dashed black curve is for the case with $n_{sen} = 1$, and the solid blue curves with increasing peak wavelength are for the cases with increasing n_{sen}, with incremental step of 0.05. (b),(d) Sensitivity and FOM versus n_{sen}, which are plotted as black and blue lines, corresponding to the left and right y axes, respectively. (a),(b) Numerical results for s polarization and (c),(d) numerical results for p polarization, with θ_{in} being 21° and 5°, respectively.

the band structure, which is very near the folded light cone. Thus, the wavelength at the resonant peak can be approximately given by the crossing between the light line and the folded light cone, i.e., $\lambda_{peak} = a(n_{sen} + \sin\theta_{in})$. The sensitivity $S = a$ r.i.u.$^{-1} = 333$ nm/r.i.u. (where "r.i.u." means "refractive index unit"). The quasi-BIC at the red section of the band structure has a large Q factor, so the FWHM of the resonant peak is small, which results in a large FOM. The numerical result for the reflectance spectrum with varied n_{sen} is plotted in Fig. 4(a). As n_{sen} increases from 1 to 1.06, the sensitivity sharply increases from 115 to 333 nm/r.i.u.; as n_{sen} further increases to 1.4, the sensitivity remains at 333 nm/r.i.u., as shown by the black line in Fig. 4(b). As n_{sen} increases from 1 to 1.13, the FOM sharply increases from 2.3×10^2 to 3.7×10^8 r.i.u.$^{-1}$; as n_{sen} further increases to 1.4, the FOM slowly decreases to 6×10^7 r.i.u.$^{-1}$, as shown by the blue line in Fig. 4(b). As a result, the sensing range within $n_{sen} \in [1, 1.4]$ has a large FOM, which can be applied for sensing of the refractive index of a gas, liquid, or biosolution.

For the p-polarized wave with $n_{sen} = 1$, the accidental BIC appears at $\theta_{in} = 9°$ and $\lambda = 506$ nm. If θ_{in} is fixed at 5°, which is near 9°, the quasi-BIC with a moderate Q factor is excited, as shown by the dashed black line in Fig. 4(c). As n_{sen} increases, the peak shifts to longer wavelength with a linear incremental shift, so the sensitivity is linearly dependent on n_{sen}, as shown by the black line in Fig. 4(d). As n_{sen} increases, the FWHM slowly increases, so the FOM slowly decreases from 1.6×10^3 to 1.4×10^2 r.i.u.$^{-1}$, as shown by the blue line in Fig. 4(d). Because the field pattern of the p-polarized quasi-BICs is localized within the dielectric slab, the sensitivity is smaller than that of the s-polarized quasi-BICs.

III. OPTICAL RESPONSE UNDER GAUSSIAN-BEAM INCIDENCE

In this section, we consider an incident Gaussian beam with finite beam width in the x-z plane but infinite beam width along the y axis (i.e., the field is uniform along the y direction). For a Gaussian beam with fixed wavelength and beam width, the field profile in the x-z plane is given as

$$\mathbf{E}_0(\rho,\eta) = \mathbf{E}_{g0}\sqrt{\frac{w_0}{w(\xi)}}e^{-\frac{\rho^2}{w^2(\xi)}+ik_0\xi+ik_0\frac{\rho^2}{2R(\xi)}-\frac{i}{2}\eta(\xi)}, \quad (3)$$

where $\xi = (\mathbf{r} - \mathbf{r}_{p0}) \cdot \mathbf{k}_{inc}$, $\rho = |\mathbf{r} - \mathbf{r}_{p0} - \xi\mathbf{k}_{inc}|$, $w(\xi) = w_0\sqrt{1 + (\xi/z_0)^2}$, $R(\xi) = \xi[1 + (z_0/\xi)^2]$, $\eta(\xi) = \tan^{-1}(\xi/z_0)$, and $z_0 = k_0 w_0^2/2$, with w_0 being the beam width

at the beam waist, $\mathbf{r}_{p0}$ being the location of the focus point, $\mathbf{k}_{\rm inc} = -\cos\theta_{\rm inc}\hat{z} + \sin\theta_{\rm inc}\hat{x}$ being the unit vector along the incident direction $\theta_{\rm inc}$, and $\mathbf{E}_{g0} = E_{y0}\hat{y}$, with E_{y0} being the amplitude of the Gaussian beam. The focus of the beam is at the top surface of the wavy dielectric slab, given as $\mathbf{r}_{p0} = \hat{x}(30a - h/2)\tan\theta_{\rm inc} + \hat{z}h/2$. Performing Fourier transformation of the field profile near to $\mathbf{r}_{p0}$, we can expand the Gaussian beam into a superposition of a series of plane waves with the same wavelength and differing incident angle. The incident angular spectrum is given by the Gaussian function $\Theta(\theta) = e^{-[(\theta-\theta_{\rm inc})/\Delta\theta_{\rm in}]^2/2}$, with $\Delta\theta_{\rm in} = \sin^{-1}[\lambda/(\sqrt{2}\pi w_0)]$ being the divergence angle. Thus, the scattering of the Gaussian beam can be decomposed into scattering of a series of plane waves with the same wavelength, differing incident angle and differing amplitude. According to the stationary-phase method, the Goos-Hänchen shifts for the Gaussian beam with $\Delta\theta_{\rm in}$ being infinitely small are given as [27]

$$S_{\rm GH} = -\frac{\lambda}{2\pi}\frac{\partial\varphi_r(\varphi_t)}{\partial\theta_{\rm in}}, \tag{4}$$

where $\varphi_r(\varphi_t)$ is the phase of the reflected (transmitted) wave. $\varphi_r(\varphi_t)$ can be extracted from the field pattern at the top (bottom) boundary of the computational domain in the simulation of plane-wave incidence by application of the spectral-element method. On the other hand, $\varphi_r(\varphi_t)$ can also be calculated by application of the multiple-layer rigorous-coupled-wave-analysis method [49]. We have confirmed that the numerical results for $\varphi_r(\varphi_t)$ given by the two methods are identical.

For a realistic structure, N_t is finite. In the numerical simulation, the flat dielectric slab in the region $|x| > N_t a$ extends into the perfectly-matched-layer region. Thus, the calculated model simulated the structure of a wavy dielectric grating with a finite number of periods, whose left and right terminations are connected to an infinitely long flat dielectric slab in the background.

A. *s* polarization

For *s* polarization, the quasi-BIC at $\lambda = 465$ nm is simulated. The reflectance (transmittance) angular spectra is plotted in Fig. 5(a), which exhibits a Fano line shape. The linewidth of the reflectance peak is defined in two ways. The Fano linewidth is defined as the difference between $\theta_{\rm in}$ with reflectance being zero and 1, which is 0.08373°. The FWHM is defined as the difference

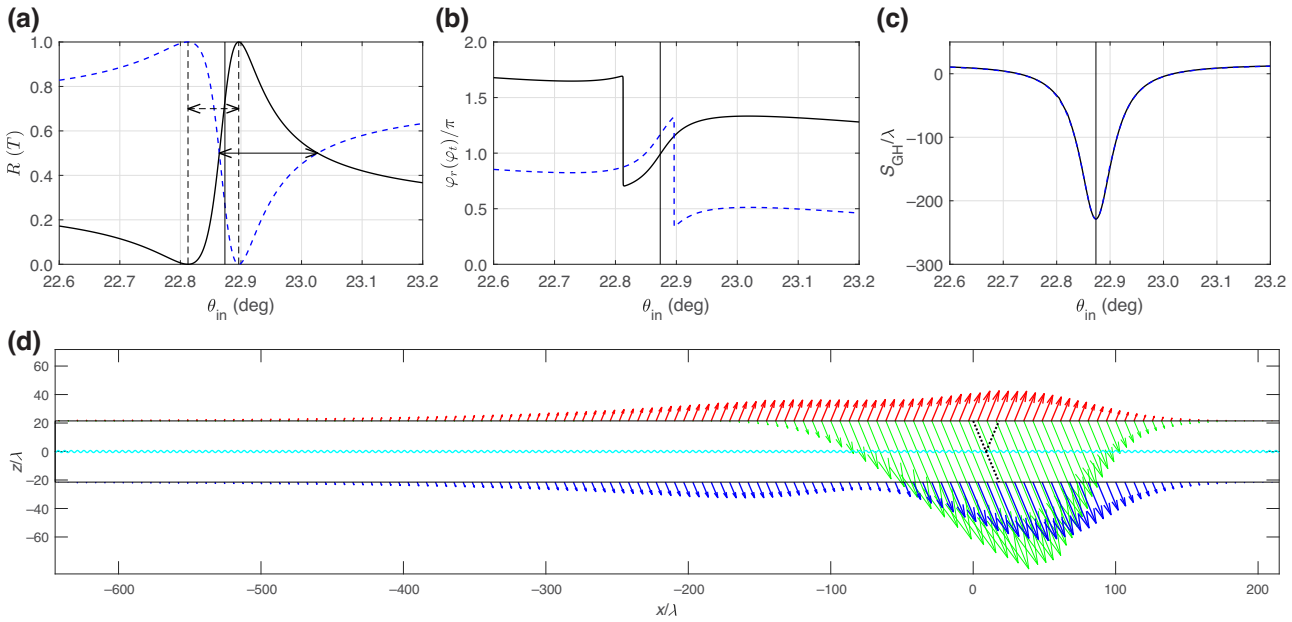

FIG. 5. (a) For *s* polarization, reflectance (transmittance) angular spectra for a quasi-BIC with $\lambda = 465$ nm plotted as a solid black line (dashed blue line). (b) Corresponding reflection-phase (transmission phase) angular spectra. (c) Corresponding Goos-Hänchen-shift angular spectra. The incident angles with maximum Goos-Hänchen shift are marked by a vertical thin solid line in (a)–(c). The incident angles with reflectance of zero and 1 are marked by vertical thin dashed lines in (a). The FWHM and Fano linewidth are marked by horizontal solid and dashed double arrows, respectively. (d) For a Gaussian beam with $\lambda = 465$ nm, $\theta_{\rm inc} = 22.8735°$, and $w_0 = 100\lambda$, spatial distribution of the time-averaged Poynting vector of the incident and the reflected fields along the horizontal observation plane that is $30a$ above the wavy top surface plotted as green and red arrows, and spatial distribution of the transmitted field along the horizontal observation plane that is $30a$ below the wavy top surface plotted as blue arrows. The axis of the incident and normal reflected beams is plotted as a thick dashed line. The horizontal cyan wavy curve indicate the location of the wavy dielectric grating.

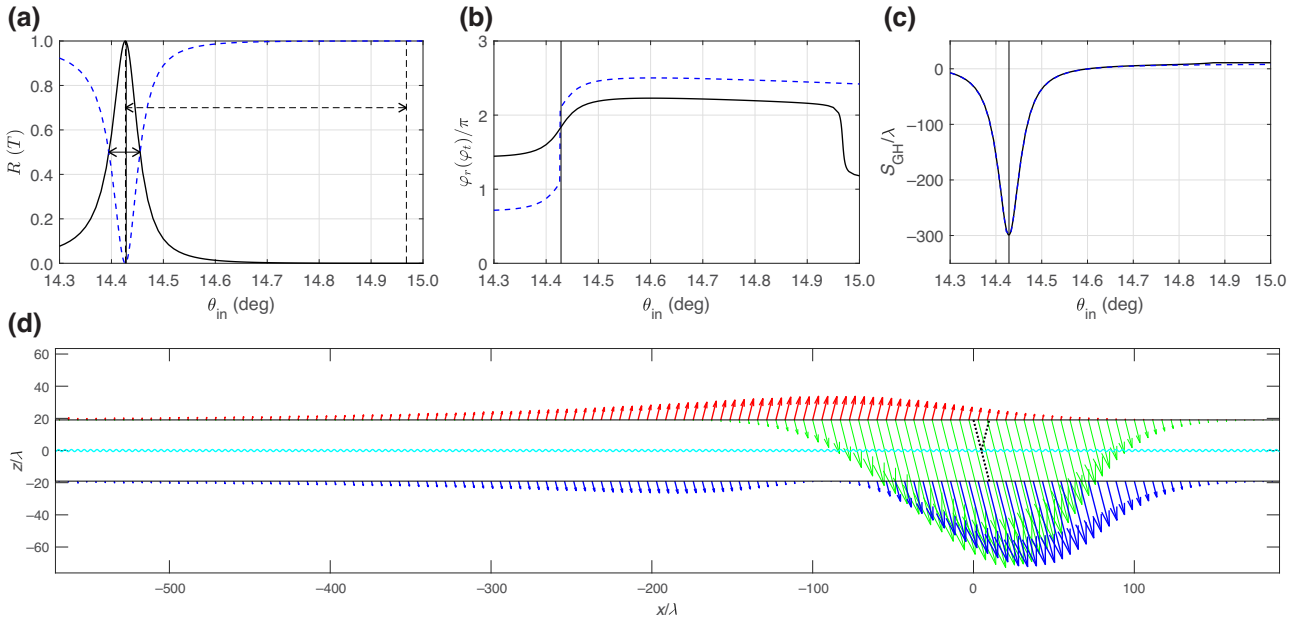

FIG. 6. Same as Fig. 5, except that the incident field is p polarized with $\lambda = 525$ nm. In (d), $\theta_{inc} = 14.4285°$.

between θ_{in} with reflectance being 0.5, which is 0.1625°. The FWHM is larger than the Fano linewidth, so the line shape is highly asymmetric. The reflection-phase (transmission-phase) angular spectra and the corresponding Goos-Hänchen-shift angular spectra are plotted in Figs. 5(b) and 5(c), respectively. At θ_{in} with reflectance (transmittance) being zero, the reflection (transmission) phase has a jump of π, so the derivatives of the phase against θ_{in}, and then the corresponding Goos-Hänchen shift at the corresponding θ_{in}, are not well defined. As $\theta_{in} \in [22.73°, 23.01°]$, the Goos-Hänchen shift is negative. The maximum magnitude of the negative Goos-Hänchen shift is 229λ at $\theta_{in} = 22.8735°$. The corresponding θ_{in} is marked by a vertical thin solid line in Figs. 5(a)–5(c), which shows that the corresponding reflectance is 0.732.

In the simulation of a Gaussian beam incident with finite beam width, θ_{inc} equates to θ_{in} with maximum magnitude of the negative Goos-Hänchen shift. For a Gaussian beam with $w_0 = 100\lambda$, the divergence angle, i.e., $2\Delta\theta_{in} = 0.2579°$, is larger than the Fano linewidth and the FWHM. The angular spectra of the reflected and transmitted beams equate to multiplication between the incident angular spectrum and the reflected and transmitted angular spectra, respectively. Within the angular spectra of the reflected and transmitted beams, the amplitude in a large range of θ_{in} with $S_{GH} > 0$ is sizable. As a result, the reflected beam consists of two parallel beams, one of which has a small positive Goos-Hänchen shift, and the other has a large negative Goos-Hänchen shift, as schematically indicated by the beams with power flux $P_{r,+}$ and $P_{r,-}$, respectively, in Fig. 1(a). Similarly, the transmitted beam also consists of two parallel beams. Because N_t is finite, before being radiated to the reflected (transmitted) beam, part of the energy of the quasi-BIC is coupled into the left flat dielectric slab with energy flux P_{WG}, as schematically indicated in Fig. 1(a). The calculated result for a system with $N_t = 900$ is plotted in Fig. 5(d), which shows that the reflected (transmitted) beam consists of two overlapping parallel beams with opposite Goos-Hänchen shifts. Because θ_{inc} is at the highly asymmetric part of the Fano line shape, the reflected beam with a large negative Goos-Hänchen shift has a large beam width and large overlap with the another reflected beam with a small positive Goos-Hänchen shift. Because N_t is large enough, P_{WG} is negligible.

The numerical Goos-Hänchen shifts of the reflected and transmitted beams can be approximated as the distance between the coordinate of the regular beam center and the coordinate with local maximum energy flux at an observation plane outside the wavy dielectric slab. By extraction of the numerical result in Fig. 5(d), for the reflected beam, the Goos-Hänchen shift of the beam with the smaller energy flux is -131λ, and that of the beam with the larger energy flux is nearly zero. For the transmitted beam, the Goos-Hänchen shift of the beam with the smaller energy flux is -182λ, and that of the beam with the larger energy flux is 17λ. The numerical results are close to the values of S_{GH} given by the stationary-phase method in Fig. 5(c).

B. p polarization

For p polarization, we simulate the quasi-BIC at $\lambda = 525$ nm. The same set of numerical results as for s polarization are plotted for p polarization in Fig. 6. The Fano line shape of the p-polarized quasi-BIC is very different

from that of the s-polarized quasi-BIC. The Fano linewidth (0.5410°) is much larger than the FWHM (0.06000°). Thus, the Fano line shape is nearly symmetric about θ_{in} with reflectance of 1. θ_{in} with maximum magnitude of the negative Goos-Hänchen shift is nearly the same as θ_{in} with reflectance of 1. As a result, the reflected beam consists mainly of a beam with a negative Goos-Hänchen shift. For the transmitted beam, the two parallel beams with positive and negative Goos-Hänchen shifts are well separated, as shown in Fig. 6(d).

By extraction of the numerical result in Fig. 6(d), the Goos-Hänchen shift of the reflected beam is -108λ. For the transmitted beam, the Goos-Hänchen shift of the beam with the smaller energy flux is -195λ, and that of the beam with the larger energy flux is 10λ. Because the FWHM is much smaller than the divergence angle of the incident Gaussian beam, i.e., $\Delta\theta_{\text{in}}$, only a small portion of the incident angular spectrum has a large negative Goos-Hänchen shift. By averaging the Goos-Hänchen shift of the whole incident angular spectrum, we find that the negative Goos-Hänchen shift of the Gaussian beam is only two thirds of the theoretical value of S_{GH} at the resonant peak in Fig. 6(c). If the beam width of the Gaussian beam is further increased, which in turn decreases $\Delta\theta_{\text{in}}$, the numerical negative Goos-Hänchen shift further approaches the theoretical value in Fig. 6(c).

C. Sensing of a device with small N_t

According to the numerical results in Figs. 5 and 6, the magnitude of the negative Goos-Hänchen shift is larger than the beam width of the Gaussian beam, i.e., w_0. Specifically, the magnitude of the negative Goos-Hänchen shift of the transmitted beam, designated as S^t_{GH}, is nearly double w_0. Thus, at $x = -|S^t_{\text{GH}}|$, the energy flux along the $-\hat{x}$ direction within the wavy dielectric grating is sizable, and the magnitude of the incident Gaussian beam is small. If the wavy shape terminates at $x = -|S^t_{\text{GH}}|$, the termination of the wavy shape has a negligible impact on the overlap between the wavy dielectric grating and the incident Gaussian beam. Thus, the energy flux at $x = -|S^t_{GH}|$ remains sizable, so a sizable energy flux could be coupled into the flat dielectric slab, i.e., P_{WG} is sizable. As a result, P_{WG} can be applied as a signal for sensing of n_{sen}. For the systems in Figs. 5(d) and 6(d), with N_t decreased to be 254 and 307, the wavy shape terminates at $x = -N_t a = -|S^t_{\text{GH}}|$, with S^t_{GH} being the corresponding negative Goos-Hänchen shift of the transmitted beam. For the s-polarized and p-polarized cases, P_{WG}/P_i is 0.276 and 0.244, respectively, with P_i being the power of the incident Gaussian beam. As n_{sen} increases, the parameters of the BIC (i.e., k_x and frequency) change, so the angular spectrum of reflectance and transmittance with a fixed incident wavelength changes. The angular Fano line shape of the quasi-BIC at the incident wavelength shifts away from the incident angle of the Gaussian beam, i.e., θ_{inc}. In other words, within the range of the angular spectrum of the incident Gaussian beam $[\theta_{\text{inc}} - \Delta\theta_{\text{in}}, \theta_{\text{inc}} + \Delta\theta_{\text{in}}]$, the magnitude of the negative Goos-Hänchen shift given by the stationary-phase method becomes smaller. Thus, the energy tunneling into the left flat dielectric slab becomes smaller, i.e., P_{WG} becomes smaller. P_{WG}/P_i versus n_{sen} is plotted in Fig. 7.

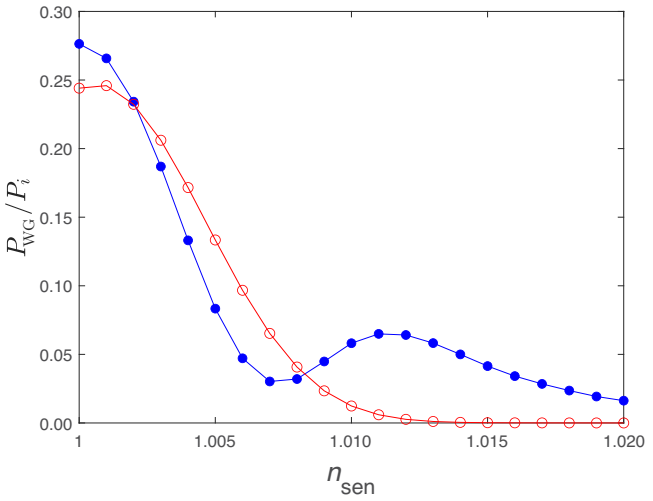

FIG. 7. For a wavy dielectric grating with $N_t = 254$ and $N_t = 307$, P_{WG}/P_i under incidence of an s-polarized and a p-polarized Gaussian beam versus n_{sen} plotted as solid blue and empty red circles, respectively. The parameters of the s-polarized and p-polarized Gaussian beams are the same as those in Figs. 5(d) and 6(d), respectively.

For s polarization, P_{WG}/P_i monotonically decreases within the range of $n_{\text{sen}} \in [1, 1.007]$, but increases as n_{sen} further increases. The oscillating behavior of P_{WG}/P_i is due to the interference between the reflected (transmitted) beams with positive and negative Goos-Hänchen shifts. The sensitivity of the sensor can be defined as the magnitude of the slope of the function P_{WG}/P_i versus n_{sen}. The sensitivity of P_{WG}/P_i versus n_{sen} can be defined as $(1/P_i)(dP_{\text{WG}}/dn_{\text{air}})$. Within the range of $n_{\text{sen}} \in [1.002, 1.005]$, P_{WG}/P_i is nearly a linear function of n_{sen}, with sensitivity being 53.83 r.i.u.$^{-1}$.

For p polarization, P_{WG}/P_i is a monotonically decreasing function of n_{sen} within the whole range of $n_{\text{sen}} \in [1, 1.02]$. In this case, the reflected (transmitted) beams with positive and negative Goos-Hänchen shifts are well separated, so the interference effect is absent. Thus, P_{WG}/P_i does not have oscillating behavior. Within the range of $n_{\text{sen}} \in [1.003, 1.007]$, P_{WG}/P_i is nearly a linear function of n_{sen}, with sensitivity being 38.20 RIU^{-1}.

To extend the sensing range of n_{sen}, the parameters of the incident Gaussian beam, i.e., λ and θ_{inc}, can be engineered so that the quasi-BIC of the systems with differing values of n_{sen} can be excited. For example, if the refractive index

n_{sen} is within the range [1.33, 1.331], one can firstly calculate the wavelength and k_x of the cutoff BIC and accidental BIC for the system with $n_{sen} = 1.33$; secondly, one can find the parameters λ and θ_{in} of the corresponding quasi-BIC with large negative Goos-Hänchen shifts. For the incident Gaussian beam, the incident angle θ_{inc} is equal to θ_{in} with maximum magnitude of the negative Goos-Hänchen shift, so P_{WG}/P_i is sizable. As n_{sen} increases from 1.33 to 1.331, P_{WG}/P_i decreases to zero due to the change of the magnitude of the Goos-Hänchen shift. Thus, the sensing range is extended to be [1.33, 1.331]. In practice, for systems with differing values of n_{sen}, a database of quasi-BICs with negative Goos-Hänchen shift of $-N_t a$ can be built. The sensor can combine the parameters (λ and θ_{inc}) of the incident Gaussian beam and the measured signal (P_{WG}/P_i) to infer the value of n_{sen}.

IV. CONCLUSION

In conclusion, the *s*-polarized and *p*-polarized reflectance spectra of a wavy dielectric grating are investigated. The cutoff BIC, which originates from the coupling between the cutoff waveguide modes and the propagating mode at the light cone, is identified. Under plane-wave incidence with wavelength below 500 nm, the sensitivity and FOM of the reflectance spectra to the refractive index of the background medium reach up to 330 nm/r.i.u. and 3.7×10^8 r.i.u.$^{-1}$, respectively. The Goos-Hänchen shifts of the corresponding quasi-BICs are calculated by our applying the stationary-phase method to the incident-plane-wave simulation, and by numerical extraction from the incident-Gaussian-beam simulation. The magnitude of the negative Goos-Hänchen shifts is around 200λ for the selected quasi-BICs. In the systems with $N_t a$ being equal to the magnitude of the numerical negative Goos-Hänchen shift, the tunneling energy flux to the flat dielectric slab is highly sensitive to the refractive index of the background medium. As a result, the system can be applied to build a refractive index sensor, which can be integrated with a dielectric waveguide in a photonic circuit.

ACKNOWLEDGMENTS

This project was supported by the Natural Science Foundation of Guangdong Province of China (Grant No. 2022A1515011578), the Special Projects in Key Fields of Ordinary Universities in Guangdong Province (New Generation Information Technology, Grant No. 2023ZDZX1007), the Project of Educational Commission of Guangdong Province of China (Grant No. 2021KTSCX064), and the Startup Grant at Guangdong Polytechnic Normal University (Grant No. 2021SDKYA117).

[1] X. Wang, M. Sang, W. Yuan, Y. Nie, and H. Luo, Optical relative humidity sensing based on oscillating wave-enhanced Goos-Hänchen shift, IEEE Photonics Technol. Lett. **28**, 264 (2016).
[2] X. Qing and M. H. Sani, Optical refractive index sensor for detection of N_2, He and CO_2 gases based on square resonance nanocavity in 2D photonic crystal, Opt. Commun. **490**, 126940 (2021).
[3] J. G. Rivas, M. Kuttge, P. H. Bolivar, H. Kurz, and J. A. Sánchez-Gil, Propagation of surface plasmon polaritons on semiconductor gratings, Phys. Rev. Lett. **93**, 256804 (2004).
[4] M. Piliarik and J. Homola, Surface plasmon resonance (SPR) sensors: Approaching their limits, Opt. Express **17**, 16505 (2009).
[5] J. Zhang, L. Zhang, and W. Xu, Surface plasmon polaritons: Physics and applications, J. Phys. D: Appl. Phys. **45**, 113001 (2012).
[6] J. Parsons, E. Hendry, C. P. Burrows, B. Auguié, J. R. Sambles, and W. L. Barnes, Localized surface-plasmon resonances in periodic nondiffracting metallic nanoparticle and nanohole arrays, Phys. Rev. B **79**, 073412 (2009).
[7] K. M. Mayer and J. H. Hafner, Localized surface plasmon resonance sensors, Chem. Rev. **111**, 3828 (2011).
[8] J. Henzie, M. H. Lee, and T. W. Odom, Multiscale patterning of plasmonic metamaterials, Nat. Nanotechnol. **2**, 549 (2007).
[9] M. Chamanzar, M. Soltani, B. Momeni, S. Yegnanarayanan, and A. Adibi, Hybrid photonic surface-plasmon-polariton ring resonators for sensing applications, Appl. Phys. B **101**, 263 (2010).
[10] S. Joseph, S. Sarkar, and J. Joseph, Grating-coupled surface plasmon-polariton sensing at a flat metal–analyte interface in a hybrid-configuration, ACS Appl. Mater. Interfaces **12**, 46519 (2020).
[11] J. Becker, A. Trügler, A. Jakab, U. Hohenester, and C. Sönnichsen, The optimal aspect ratio of gold nanorods for plasmonic bio-sensing, Plasmonics **5**, 161 (2010).
[12] W. Li, X. Jiang, J. Xue, Z. Zhou, and J. Zhou, Antibody modified gold nano-mushroom arrays for rapid detection of alpha-fetoprotein, Biosens. Bioelectron. **68**, 468 (2015).
[13] L. Shi, J. Shang, Z. Liu, Y. Li, G. Fu, X. Liu, P. Pan, H. Luo, and G. Liu, Ultra-narrow multi-band polarization-insensitive plasmonic perfect absorber for sensing, Nanotechnology **31**, 465501 (2020).
[14] P. B. Johnson and R. W. Christy, Optical constants of the noble metals, Phys. Rev. B **6**, 4370 (1972).
[15] F. Wu, M. Qin, and S. Xiao, Quasi-bound state in the continuum supported by a compound grating waveguide structure for high-figure-of-merit refractive-index sensing, J. Appl. Phys. **132**, 193101 (2022).
[16] A. F. Sadreev, Interference traps waves in an open system: Bound states in the continuum, Rep. Prog. Phys. **84**, 055901 (2021).
[17] C. W. Hsu, B. Zhen, A. D. Stone, J. D. Joannopoulos, and M. Soljačić, Bound states in the continuum, Nat. Rev. Mater. **1**, 16048 (2016).
[18] D. C. Marinica, A. G. Borisov, and S. V. Shabanov, Bound states in the continuum in photonics, Phys. Rev. Lett. **100**, 183902 (2008).

[19] E. N. Bulgakov and A. F. Sadreev, Bound states in the continuum in photonic waveguides inspired by defects, Phys. Rev. B **78**, 075105 (2008).
[20] Y. Plotnik, O. Peleg, F. Dreisow, M. Heinrich, S. Nolte, A. Szameit, and M. Segev, Experimental observation of optical bound states in the continuum, Phys. Rev. Lett. **107**, 183901 (2011).
[21] B. Zhen, C. W. Hsu, L. Lu, A. D. Stone, and M. Soljačić, Topological nature of optical bound states in the continuum, Phys. Rev. Lett. **113**, 257401 (2014).
[22] Y. Yang, C. Peng, Y. Liang, Z. Li, and S. Noda, Analytical perspective for bound states in the continuum in photonic crystal slabs, Phys. Rev. Lett. **113**, 037401 (2014).
[23] T. Xu, M. S. Wheeler, S. V. Nair, H. E. Ruda, M. Mojahedi, and J. S. Aitchison, Highly confined mode above the light line in a two-dimensional photonic crystal slab, Appl. Phys. Lett. **93**, 241105 (2008).
[24] J. Lee, B. Zhen, S.-L. Chua, W. Qiu, J. D. Joannopoulos, M. Soljačić, and O. Shapira, Observation and differentiation of unique high-Q optical resonances near zero wave vector in macroscopic photonic crystal slabs, Phys. Rev. Lett. **109**, 067401 (2012).
[25] K. Koshelev, S. Lepeshov, M. Liu, A. Bogdanov, and Y. Kivshar, Asymmetric metasurfaces with high-Q resonances governed by bound states in the continuum, Phys. Rev. Lett. **121**, 193903 (2018).
[26] F. Goos and H. Hänchen, Ein neuer und fundamentaler Versuch zur Totalreflexion, Ann. Phys. **436**, 333 (1947).
[27] K. Artmann, Berechnung der Seitenversetzung des totalreflektierten Strahles, Ann. Phys. **437**, 87 (1948).
[28] R. Kaiser, Y. Levy, J. Fleming, S. Muniz, and V. S. Bagnato, Resonances in a single thin dielectric layer: Enhancement of the Goos-Hänchen shift, Pure Appl. Opt. **5**, 891 (1996).
[29] X. Yin, L. Hesselink, Z. Liu, N. Fang, and X. Zhang, Large positive and negative lateral optical beam displacements due to surface plasmon resonance, Appl. Phys. Lett. **85**, 372 (2004).
[30] Y. Wang, H. Li, Z. Cao, T. Yu, Q. Shen, and Y. He, Oscillating wave sensor based on the Goos-Hänchen effect, Appl. Phys. Lett. **92**, 061117 (2017).
[31] Y. Xu, C. T. Chan, and H. Chen, Goos-Hänchen effect in epsilon-near-zero metamaterials, Sci. Rep. **5**, 8681 (2015).
[32] J. Wen, J. Zhang, L. Wang, and S. Zhu, Goos-Hänchen shifts in an epsilon-near-zero slab, J. Opt. Soc. Am. B **34**, 2310 (2017).
[33] L. Wang and S. Zhu, Giant lateral shift of a light beam at the defect mode in one-dimensional photonic crystals, Opt. Lett. **31**, 101 (2006).
[34] J. Wu, F. Wu, K. Lv, Z. Guo, H. Jiang, Y. Sun, Y. Li, and H. Chen, Giant Goos-Hänchen shift with a high reflectance assisted by interface states in photonic heterostructures, Phys. Rev. A **101**, 053838 (2020).
[35] Y. Chen, Y. Ban, Q. Zhu, and X. Chen, Graphene-assisted resonant transmission and enhanced Goos-Hänchen shift in a frustrated total internal reflection configuration, Opt. Lett. **41**, 4468 (2016).
[36] W. Zhen and D. Deng, Goos-Hänchen shifts for Airy beams impinging on graphene-substrate surfaces, Opt. Express **28**, 24104 (2020).
[37] M. Luo and F. Wu, Wavy optical grating: Wideband reflector and Fabry-Pérot bound states in the continuum, Phys. Rev. A **106**, 063514 (2022).
[38] F. Wu, J. Wu, Z. Guo, H. Jiang, Y. Sun, Y. Li, J. Ren, and H. Chen, Giant enhancement of the Goos-Hänchen shift Assisted by quasibound states in the continuum, Phys. Rev. Appl. **12**, 014028 (2019).
[39] F. Wu, M. Luo, J. Wu, C. Fan, X. Qi, Y. Jian, D. Liu, S. Xiao, G. Chen, H. Jiang, Y. Sun, and H. Chen, Dual quasibound states in the continuum in compound grating waveguide structures for large positive and negative Goos-Hänchen shifts with perfect reflection, Phys. Rev. A **104**, 023518 (2021).
[40] M. S. Kirsch, Y. Zhang, M. Kremer, L. J. Maczewsky, S. K. Ivanov, Y. V. Kartashov, L. Torner, D. Bauer, A. Szameit, and M. Heinrich, Nonlinear second-order photonic topological insulators, Nat. Phys. **17**, 995 (2021).
[41] M. Luo and Q. H. Liu, Extraordinary transmission of a thick film with a periodic structure consisting of strongly dispersive materials, J. Opt. Soc. Am. B **28**, 629 (2011).
[42] M. Luo and Q. H. Liu, Three-dimensional dispersive metallic photonic crystals with a bandgap and a high cutoff frequency, J. Opt. Soc. Am. A **27**, 1878 (2010).
[43] M. Luo, Q. H. Liu, and J. Guo, A spectral element method calculation of extraordinary light transmission through periodic subwavelength slits, J. Opt. Soc. Am. B **27**, 560 (2010).
[44] M. Luo and Q. H. Liu, Accurate determination of band structures of 2D dispersive anisotropic photonic crystals by the spectral element method, J. Opt. Soc. Am. A **26**, 1598 (2009).
[45] M. Luo and Q. H. Liu, Spectral element method for band structures of three-dimensional anisotropic photonic crystals, Phys. Rev. E **80**, 056702 (2009).
[46] M. Luo, Q. H. Liu, and Z. Li, Spectral element method for band structures of two-dimensional anisotropic photonic crystals, Phys. Rev. E **79**, 026705 (2009).
[47] S. Romano, G. Zito, S. Torino, G. Calafiore, E. Penzo, G. Coppola, S. Cabrini, I. Rendina, and V. Mocella, Label-free sensing of ultralow-weight molecules with all-dielectric metasurfaces supporting bound states in the continuum, Photonics Res. **6**, 726 (2018).
[48] D. N. Maksimov, V. S. Gerasimov, S. Romano, and S. P. Polyutov, Refractive index sensing with optical bound states in the continuum, Opt. Express **28**, 38907 (2020).
[49] M. G. Moharam, D. A. Pommet, E. B. Grann, and T. K. Gaylord, Stable implementation of the rigorous coupled-wave analysis for surface-relief gratings: Enhanced transmittance matrix approach, J. Opt. Soc. Am. A **12**, 1077 (1995).